In vivo targeting and multimodal imaging of cerebral amyloid-β aggregates using hybrid GdF 3 nanoparticles

Frédéric Lerouge, Elodie Ong, Hugo Rositi, Francis Mpambani, Lise-Prune Berner, Radu Bolbos, Cécile Olivier, Françoise Peyrin, Vinu K Apputukan, Cyrille Monnereau, et al.

Research Article

For reprint orders, please contact: reprints@futuremedicine.com

Nanomedicine

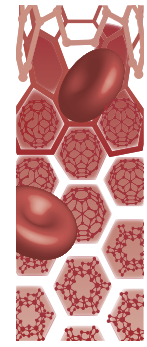

In vivo targeting and multimodal imaging of cerebral amyloid-β aggregates using hybrid GdF_3 nanoparticles

Frédéric Lerouge[‡,1], Elodie Ong[‡,2], Hugo Rositi[3], Francis M Pambani[1], Lise-Prune Berner[4], Radu Bolbos[5], Cécile Olivier[4], Françoise Peyrin[4], Vinu Apputukan[1], Cyrille Monnereau[1], Chantal Andraud[1], Frederic Chaput[1], Yves Berthezène[4], Bettina Braun[6], Mathias Jucker[6], Andreas KO Åslund[7], Sofie Nyström[7], Per Hammarström[7], K Peter R Nilsson[7], Mikael Lindgren[8], Marlène Wiart[9,10], Fabien Chauveau*[,§,2] & Stephane Parola**[,§,1]

[1]Univ. Lyon, École Normale Supérieure de Lyon, Laboratoire de Chimie; Univ. Lyon 1; CNRS UMR 5182, Lyon, France
[2]Univ. Lyon, Lyon Neuroscience Research Center; CNRS UMR5292; INSERM U1028; Univ. Lyon 1, Lyon, France
[3]Univ. Clermont Auvergne, Institut Pascal; CNRS UMR 6602; SIGMA Clermont, Clermont-Ferrand, France
[4]Univ. Lyon, CREATIS; INSA-Lyon; Univ. Lyon 1; CNRS UMR5220; INSERM U1206, Villeurbanne, France
[5]CERMEP, Lyon, France
[6]Department of Cellular Neurology, Hertie Institute for Clinical Brain Research, Univ Tübingen, Tübingen, Germany
[7]Department of Physics, Chemistry, & Biology, Linköping Univ, Linköping, Sweden
[8]Department of Physics, Norwegian Univ. of Science & Technology, Trondheim, Norway
[9]Univ. Lyon, CarMeN laboratory; INSERM U1060; INRA U1397; Univ. Lyon 1, INSA-Lyon, Oullins, France
[10]CNRS, Lyon, France
*Author for correspondence: Tel.: +33 472 688 629; chauveau@cermep.fr
**Author for correspondence: Tel.: +33 472 728 157; stephane.parola@ens-lyon.fr
[‡]Co-first authors
[§]Co-last authors

Aim: To propose a new multimodal imaging agent targeting amyloid-β (Aβ) plaques in Alzheimer's disease. **Materials & methods:** A new generation of hybrid contrast agents, based on gadolinium fluoride nanoparticles grafted with a pentameric luminescent-conjugated polythiophene, was designed, extensively characterized and evaluated in animal models of Alzheimer's disease through MRI, two-photon microscopy and synchrotron x-ray phase-contrast imaging. **Results & conclusion:** Two different grafting densities of luminescent-conjugated polythiophene were achieved while preserving colloidal stability and fluorescent properties, and without affecting biodistribution. *In vivo* brain uptake was dependent on the blood–brain barrier status. Nevertheless, multimodal imaging showed successful Aβ targeting in both transgenic mice and Aβ fibril-injected rats.

Plain language summary: The design and study of a new contrast agent targeting amyloid-β (Aβ) plaques in Alzheimer's disease (AD) is proposed. Aβ plaques are the earliest pathological sign of AD, silently appearing in the brain decades before the symptoms of the disease are manifested. While current detection of Aβ plaques is based on nuclear medicine (a technique using a radioactive agent), a different kind of contrast agent is here evaluated in animal models of AD. The contrast agent consists of a nanoparticle made of gadolinium and fluorine ions (core), and decorated with a molecule previously shown to bind to Aβ plaques (grafting). The core is detectable with MRI and x-ray imaging, while the grafting molecule is detectable with fluorescence imaging, thus allowing different imaging methods to be combined to study the pathology. In this work, the structure, stability and properties of the contrast agent have been verified *in vitro* (in tubes and on brain sections). Then the ability of the contrast agent to bind to Aβ plaques and provide a detectable signal in MRI, x-ray or fluorescence imaging has been demonstrated *in vivo* (in rodent models of AD). This interdisciplinary research establishes the proof of concept that this new class of versatile agent contrast can be used to target pathological processes in the brain.

Future Medicine

Tweetable abstract: New multimodal contrast agent developed at University of Lyon: a functionalized gadolinium-based nanoparticle shows successful targeting of amyloid-β fibrils and *in vivo* detection with two-photon microscopy and MRI in animal models of Alzheimer's disease.

Graphical abstract:

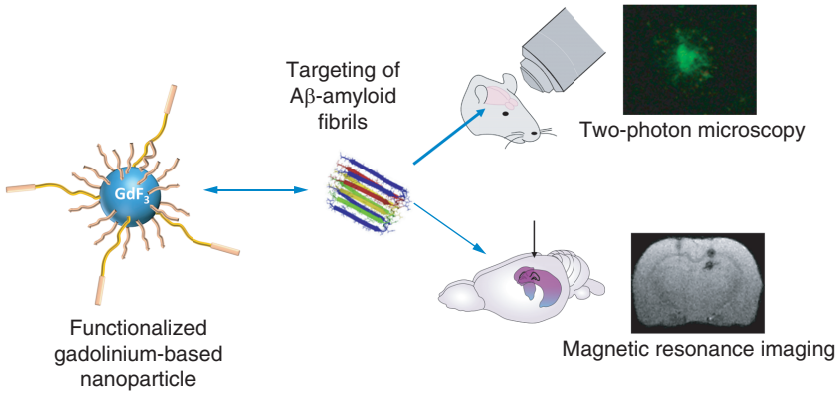

First draft submitted: 28 September 2022; Accepted for publication: 16 February 2023; Published online: TBC

Keywords: amyloid-β • gadolinium fluoride nanoparticles • luminescent-conjugated polythiophenes • multimodal imaging

Among brain pathologies, Alzheimer's disease (AD) is the most frequent cause of dementia. Amyloid-β (Aβ) fibrillation is described as a central event in the pathogenesis of AD. Amyloid imaging is expected to play a pivotal role in early and differential diagnosis of dementias, and in the evaluation of anti-Aβ treatments. PET with radiotracers that bind to Aβ fibrils has been instrumental in translational research, but has limitations (high nonspecific binding, spatial resolution in the millimeter range), especially for rodent studies [1]. As an alternative, numerous magnetic nanostructures have been proposed to visualize Aβ deposition [2,3]. In particular, ultrasmall superparamagnetic iron oxide nanoparticles have been successfully used as a T2*-weighted MRI targeted contrast agent [4–7]. On the other hand, two-photon microscopy (TPM) imaging appears to be an important technique for high-resolution imaging – though at the cost of limited tissue penetration – and luminescent conjugated polythiophenes (LCPs) were demonstrated to be efficient optical biomarkers of protein fibrillation [8].

The importance of multimodality lies in the ability to merge various technologies in order to combine their resolution and sensitivity toward multiscale imaging. Recently, we evaluated a multimodal fluorescent magnetic hybrid nanoprobe, based on gadolinium fluoride nanoparticles functionalized with such a tetramer LCP moiety [9]. *Ex vivo* imaging showed efficient staining but massive uptake in liver tissues. Here we propose the design of a new generation of markers, with LCP in its pentameric form (pentamer formyl thiophene acetic acid [p-FTAA], which showed the most efficient staining [10]), supported with a specifically designed polymeric ligand to provide better colloidal stability and enhanced blood–brain barrier (BBB) crossing. We report an extensive characterization and *in vivo* evaluation of this improved contrast agent with MRI and TPM, as well as *ex vivo* detection with synchrotron x-ray phase-contrast imaging (XPCI).

Materials & methods

Synthesis & functionalization of GdF_3 nanoparticles

The synthesis and functionalization of GdF_3 nanoparticles has already been extensively described previously [9] and is here reproduced in part, with modifications (PEG moieties and LCP derivatives). The hybrid nanoprobes consist of GdF_3 nanocrystals (see transmission electron microscopy and x-ray diffraction in Supplementary Figure 1) cofunctionalized with both PEG and multifunctional LCP derivatives (Figure 1). Both organic moieties are strongly anchored on the inorganic particles' surface through phosphonic acid functions which are known to have great interaction with gadolinium (Gd^{3+}), thus ensuring high stability of the overall systems in a biological environment. The PEG chain ensures biocompatibility and the LCP polymer, constituted of a highly efficient

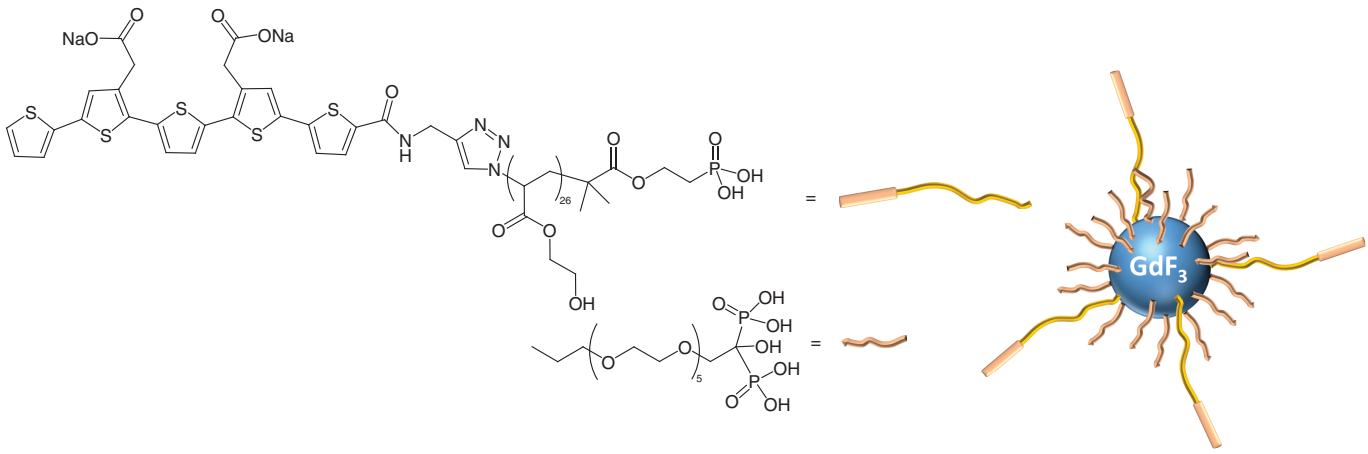

Figure 1. (Left, top) Multifunctional luminescent-conjugated polythiophene polymer bearing phosphonic acid, spacer and PEGylated luminescent-conjugated polythiophene pentamer and (Left, bottom) PEG polymer bearing bisphosphonate unit. (Right) General scheme of the multifunctional hybrid nanoprobe nanoGd (right).

polythiophene unit under its pentameric form [10], allows both targeting and imaging of amyloid aggregates. The high length of the polymer chain is designed to ensure the LCP can easily reach the targeting site within the amyloid aggregates, acting in the same way as the free LCP.

The final hybrid nanoGd were obtained following an already described process [9,11] and two different compositions were prepared with 2% and 10% of LCP polymers. In our experience, a higher grafting ratio leads to fluorophore–fluorophore and LCP–surface interactions that impact the emission properties and the targeting efficiency in a detrimental way. Functionalization of the nanoparticles was achieved by adding a suspension of 1 mmol of native GdF_3 nanoparticles in water to a mixture of 0.5 mmol of coupling molecules (bisphosphonate-PEG-CH_3 and LCP-spacer) for an overall P:Gd ratio of 1:2. After 5 h at 70°C, the obtained nanoGd (nanoGd2% or nanoGd10%) were purified by dialysis and freeze-dried before analysis and further use for *in vivo* studies.

Synthesis of the polyhydroxy methacrylate polymer

In this work, polyhydroxyethylacrylate was used, with two different lengths of 14 and 26 units. The strategy consisted in synthesizing linkers of various lengths. This was achieved using the atom transfer radical polymerization strategy (Supplementary Figure 2) for three main reasons. First, it allows, with a minimum synthetic effort, the synthesis of objects with various and very defined lengths. Second, it allows the synthesis of objects functionalized on both a and w ends, with groups allowing further coupling to the fluorescent probe (N3) and anchoring to the nanoparticles (PO_3H_2). Third, it allows the composition of the linker to be changed by varying the nature of the starting monomer material, and therefore achieving control over some crucial properties of the linker (water solubility, biocompatibility).

Clicking of the medium spacer (whose synthesis has been described elsewhere [12]) with pentameric LCP was performed as described in Supplementary Figure 3. The preparation procedure of pFTAA-p$(HEA)_{26}$-PO_3H_2 was similar to that of qFTAA-p$(HEA)_{14}$-PO_3H_2, using a longer spacer instead of the medium one and attached to the pentameric LCP (pFTAA) instead of the tetrameric one (qFTAA).

Characterization

Inductively coupled plasma measurements were performed on an axial Jobin Yvon 138 Ultrace spectrometer. An average of three measurements is used for the determination of the final values, which are back-calculated to offset the initial dilution. Individual values are obtained with a relative standard deviation of 3% or less. Fourier transform infrared (FTIR) spectroscopy in the range 500–4000 cm^{-1} was achieved on a Perkin-Elmer spectrum 100 FTIR spectrophotometer equipped with universal ATR. Dynamic light scattering experiments were performed using a Malvern Zetasizer Nano ZS. Absorption spectra were recorded on a Perkin-Elmer UV-vis-NIR Lambda 750 spectrometer.

Relaxivity constants were recorded on a 7T Bruker system. The samples were diluted in saline solutions. Concentrations were 10, 5, 2.5, 1.25, 0.625 and 0.313 mM in Gd; concentrations 2.5, 1.25, 0.625 and 0.313 mM

10.2217/nnm-2022-0252

were used for T1 measurements. Concentrations of 0.156, 0.078, 0.039 mM in Gd were used for T2 measurements. T1 was measured using spin echo sequence, TE 8.3 ms, varying TR 13 ms–6400 ms. T2 was measured using spin echo sequence, TR 15000, 16 Echoes TE = 11s–176 ms.

Quantum efficiency (QE) was measured using a Horiba Jobin Yvon Fluorolog-3® spectrofluorometer, using the Demasa and Crosby method [13]. Steady-state absorption spectra were recorded using a Shimadzu UV-1601PC spectrophotometer and photoluminescence measurements were carried out employing a PTI QuantaMaster™ 8075-22 (Horiba Scientific) equipped with Double Mono 300 spectrometer chambers for both excitation and emission. A Hamamatsu R928 PMT was used for detection in the range 185–950 nm. A OB-75X (75 W xenon arc lamp) was used as the light source. Data acquisition and basic data handling of steady-state luminescence data were carried out with the Felix Data Analysis software and further processed and presented using Origin Pro. Time-resolved fluorescence decays were recorded using an IBH time-correlated single photon counting spectrometer system with 1 nm resolved emission monochromator (5000 M, Glasgow, UK). The system was equipped with a TBX-04D picosecond photon detection module and the sample was excited using an IBH LED operating at 469 nm, setting the emission recording at 540 nm using a 16-nm slit. The measured decay trace was analyzed using deconvolution fitting with the IBH Data Station v 2.1 software.

Two-photon absorption excitation hyperspectral images

Two-photon absorption (TPA) spectral images were recorded using a Zeiss LSM510 META microscope (Carl Zeiss GmbH, Jena, Germany) equipped with a 5W Ti:Sapphire laser (MIRA, Continuum, CA, USA) delivering 200-fs pulses at 80 MHz, pulse energy of approx 5–10 nJ. A C-Apochromat 40×/1.2 W objective and the spectral META detector using 32 channels at 10.7 nm resolution in the range 377–719 nm were employed. A HFT KP 680 filter (short pass) was used to block excitation radiation. The images (512 × 512, 12-bit) were recorded by four scanned averages (3.2 ps pixel dwell time).

Animal models

All experiments were carried out under protocols approved by local ethical review boards in Lyon, France and Tübingen, Germany, and were in accordance with EU directives on the protection and use of laboratory animals (Council Directive 2010/63/EU).

Nontransgenic rat model of AD (n = 3)

Focal injection of preaggregated Aβ fibrils was performed in the hippocampus of wild-type, male Sprague Dawley rats, under isoflurane anesthesia, as previously described (0.5 nmol of preformed $A\beta_{42}$ fibrils in 5 µl in the right dentate gyrus: AP = -3.2 mm; ML = 1.2 mm; DV = -3.6 mm) [14]. Synthetic $A\beta_{42}$ fibrils were obtained from recombinant $A\beta_{42}$ (rPeptide), dissolved at 200 µM in 0.1% NH_4OH and aggregated at 37°C, 250 r.p.m. for 3 days. The formation of fibrils was controlled by transmission electron microscopy and thioflavine T spectrofluorescence.

Transgenic mouse model of AD pathology (n = 2)

Double transgenic APPPS1 mice were initially described in 2006 [15] and are listed on the Alzforum database (https://www.alzforum.org/research-models/appps1). Animals used in this study were hemizygous 11-month-old females.

Multimodal imaging

Magnetic resonance imaging

MRI was performed in mice and rats under isoflurane anesthesia on a horizontal 7T Bruker Biospec MRI system (Bruker Biospin MRI GmbH, Ettlingen, Germany) with a set of 400 mT/m gradients, controlled by a Bruker ParaVision 5.1 workstation. A respiratory sensor was placed on the abdomen to continuously monitor respiration rate on a specialized device (ECG Trigger Unit HR V2.0, Rapid Biomedical). Body temperature was maintained at 37 ± 1°C via a circuit of thermoregulated water.

For abdominal imaging in mice, the animals were placed in the supine position in a 32-mm inner diameter whole-body transmit–receive coil. The sequence was triggered on respiration. Axial T1 images were obtained with a dynamic multigradient echo 2D sequence (field of view 35 × 35 mm^2, slice thickness 1 mm, matrix 128 × 128, 37 slices, TE1-TE2/TR = 1.5–3.9/800 ms; flip angle = 70°; one average; acquisition time/frame = 1.42 min; number

of repetitions = 30). A bolus of NanoGd at the dose of 150 µmol Gd/kg was intravenously injected through the tail vein during the dynamic sequence after the acquisition of a precontrast baseline.

For brain imaging in mice and rats, the animals were placed in the prone position in a dedicated plastic bed equipped with a stereotactic holder (Bruker Biospec Animal Handling Systems). A Bruker birdcage volume coil (outer diameter = 120 mm and inner diameter = 72 mm) was used for signal emission. A Bruker single-loop surface coil (25 mm diameter for rats, 15 mm diameter for mice) was positioned on the head of the animals to target the brain, for signal reception. For mouse imaging the field of view was 20 × 20 mm^2 and the matrix was 256 × 256; 15 slices of 1-mm thickness were acquired. For T2-weighted imaging, we used a RARE spin-echo sequence (TE/TR = 69.1 mm/4000 ms, bandwidth = 25 kHz, number of averages = 2). For dynamic imaging in the mouse brain, we used a 2D multigradient echo sequence with eight echo times (TE/TR 2.0–6.3–10.6–14.8–19.1–23.4–27.7–31.9/800 ms, bandwidth = 50 kHz, flip angle = 35°, one average, acquisition time/frame = 1.42 min; number of repetitions = 40). For rat imaging, the field of view was 30 × 15 mm^2 and the matrix was 256 × 128; 15 slices of 0.8 mm thickness were acquired. For T2-weighted imaging, we used a RARE spin-echo sequence (TE/TR = 57.7/5000 ms, bandwidth = 26 kHz, four averages). For T2*-weighted imaging, we used a FLASH gradient-echo sequence (TE/TR = 20/680 ms, bandwidth = 20 kHz, flip angle = 20°, four averages).

Magnetic resonance (MR) signal changes in time were analyzed in regions of interest (ROIs) with ImageJ software (NIH, MD, USA) and expressed as a percentage of the precontrast values.

Synchrotron XPCI

Excised rat brains were conditioned for *ex vivo* XPCI: hemispheres were separated, dehydrated in successive baths of graded ethanol (25–50–75–96%) and scanned in 1-cm plastic tubes filled with ethanol. Imaging was performed at the ID19 beamline of the European Synchrotron Radiation Facility (ESRF, Grenoble, France), using the propagation-based imaging technique, which exploits free-space propagation in order to have detectable interference fringes. This innovative imaging approach allows the detection of metal-based nanoparticles as hyperintense signals while providing a unique histological contrast at the microscopic level [16,17]. Tomographic images (2000 projections during a 180° rotation in 10 min) were recorded at a single sample-detector distance (1 m) where the camera (FReLoN) was positioned away from the sample to obtain phase contrast. The acquisitions were performed with a polychromatic 'pink' incident x-ray beam (19 keV). Tomographic reconstructions with resulting 3D volumes of isotropic voxel size of 7.5 µm (1.2 × 1.2 × 1.2 cm^3 field of view, matrix 2048 × 2048, 2000 slices) were obtained using the Paganin single distance phase-retrieval approach [18] of the PyHST2 software [19], with δ/β ratio set to 1000 [20]. Images were screened for the presence of nanoparticle-related bright spots and were visually compared with corresponding MRI slices.

Two-photon microscopy

Surgery and imaging were performed as previously described [21]. Briefly, a round cranial window (4 mm diameter) was installed on the temporal cortex under general anesthesia (fentanyl, 0.05 mg/kg; midazolam, 5 mg/kg; medetomidine, 0.50 mg/kg). Without puncturing the dura mater, a sterile, custom-made glass coverslip (thickness 0.13 mm) was slowly placed and sealed to the skull with light-curing dental cement. A custom-made titanium ring (14 mm diameter) was then sealed onto the skull above the cranial window for repeatable target localization during imaging [22]. After surgery, the animals were allowed to recover for 1 week before the imaging process was started.

In vivo imaging was performed on two different locations per mouse at regular intervals. Before each imaging session, mice were anesthetized with isoflurane. The cranial window was cleaned, and the mouse was secured under the microscope by fitting the titanium ring in a custom-built head fixation apparatus connected to a motorized stage. The brain areas were chosen 1 day before the imaging with the NanoGd started, after a Texas Red injection (70 kDa; 12.5 mg/ml in sterile phosphate-buffered saline; Invitrogen, CA, USA) to visualize blood vessels and select areas of interest. All imagery was taken using a 40× HCX APO water-immersion objective (0.8 numerical aperture; Leica Microsystems, Wetzlar, Germany) under a Leica SP2 confocal microscope equipped with a Spectra Physics Mai Tai® laser (tunable 710–990 nm), which provided multiphoton excitation at 910 nm for the LCP pentamer. Intensities within Aβ plaques, vessels and parenchyma in maximum projection images were averaged (n = 3–4 each).

10.2217/nnm-2022-0252

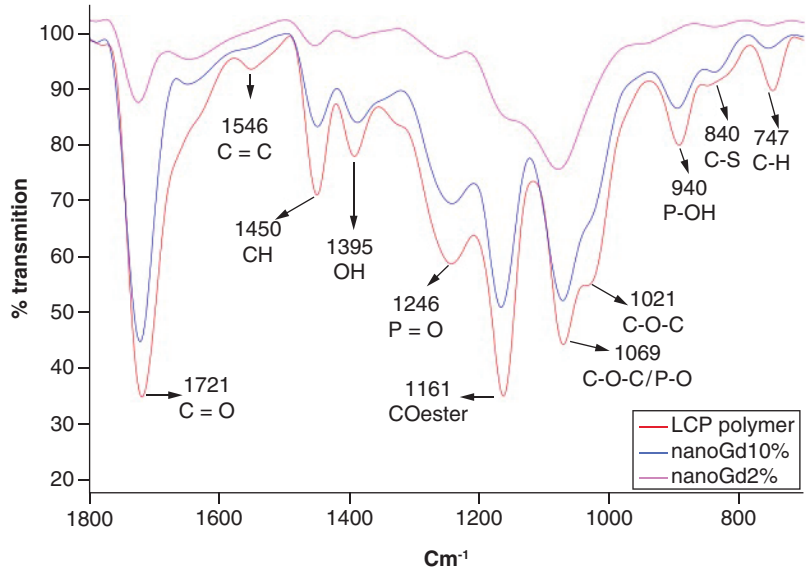

Figure 2. Fourier transform infrared of nanoGd2%, nanoGd10% and luminescent-conjugated polythiophene polymer.
LCP: Luminescent-conjugated polythiophene.

Results

Characterization

Efficient grafting was first evidenced by dynamic light scattering measurements of nanoparticle suspensions in phosphate buffer (Supplementary Figure 4). In the case of GdF_3, due to a low stability in the saline medium, the hydrodynamic diameter of the particles was previously measured in water at 32 nm. After surface modification, the nanoprobes' diameters were measured at 70 nm in the case of nanoGd2% and 46 nm in the case of nanoGd10%, proving the presence of organic moieties surrounding the inorganic core. The difference in sizes suggests a lower stability of nanoGd2% in the buffer than nanoGd10%, leading to partial aggregation; indeed, the larger the number of LCP moieties around the particles (i.e., nanoGd10% compared with nanoGd2%), the better the nanoprobe stability.

The presence of both PEG and LCP polymer on the GdF_3 surface was further verified through FTIR analysis of nanoGd2%, nanoGd10% and the LCP polymer previous to grafting. The main vibration bands are identified in Figure 2. Both nanoGd2% and nanoGd10% showed the P=O and P-O stretching bands specific to phosphonate units at 1246 and 1069 cm^{-1}. Grafting of the LCP polymers around the particles was highlighted by the bands relative to thiophene units observed at 840 and 747 cm^{-1} but also the vibrational bands relative to carboxylates on the polythiophene units at 1721 cm^{-1} (C=O). This last result proved that these polythiophene units were in their free form and not linked on the particle surface through the carboxylate groups. Inductively coupled plasma atomic emission spectrometry was used to quantify the number of ligands at the particle surface. Quantification of phosphorus gives the total amount of ligand (PEG and LCP derivatives) and quantification of sulfur allows discrimination between PEG and LCP ligands. The results showed an average of 1442 ligands (PEG and LCP) per nanoGd2% particle (2.0 ligands/nm^2) and 1559 ligands per nanoGd10% particle (2.2 ligands/nm^2) with respective PEG/LCP ratios of 3.9 and 1.4. These values, far below the theoretical ones based on introduced ratios (49 and 9), are probably due to steric hindrance of the LCP moieties reducing their interaction with the surface.

To further confirm these observations and validate the potential use of these nanoGds as contrast agents for fluorescence imaging, optical spectroscopy was carried out to compare their ability for amyloid staining with previous LCP ligands. UV/Visible absorption and fluorescence measurements comparing LCP [10] and nanoGd10% are shown in Figure 3. Upon the modification of the pentameric LCP moiety there was, firstly, a small change in the optical properties, manifested as a red shift of both the absorption and emission maxima of approximately 15–20 nm; along with, secondly, a slight broadening of the absorption band, suggesting a change in the local environment of the probes resulting from their immobilization on the surface, and possibly minor aggregation effects. Time-correlated single photon counting (Supplementary Figure 5) revealed that the lifetimes of the probes

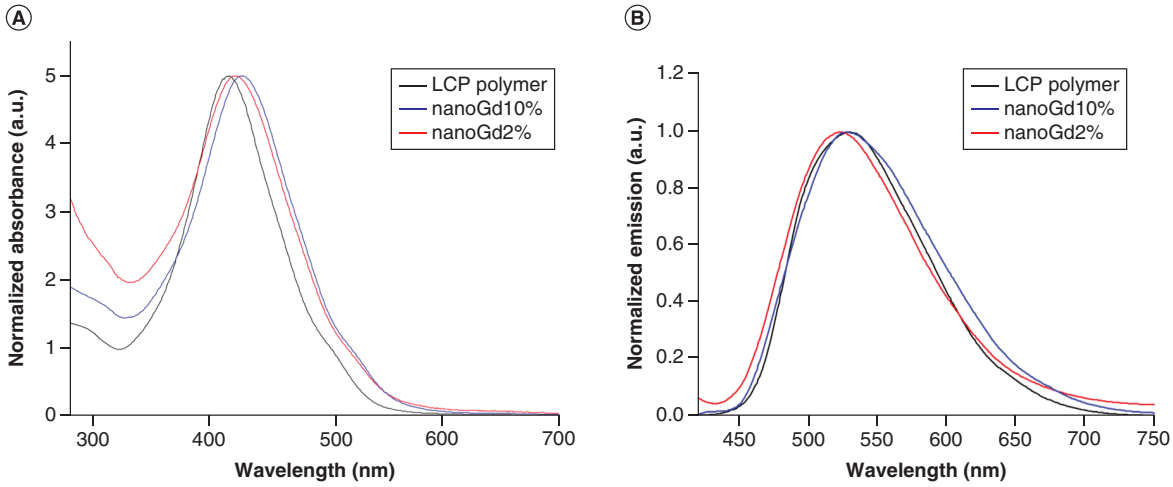

Figure 3. **(A)** UV/VIS normalized absorption spectrum of nanoprobes and free luminescent-conjugated polythiophene polymer. **(B)** Normalized fluorescence emission of nanoprobes and free LCP polymer after excitation at 420 nm.
LCP: Luminescent-conjugated polythiophene.

Table 1. Quantum efficiency of the nanoprobes and PEG–luminescent-conjugated polythiophene.

Compound	Quantum efficiency
PEG-LCP	0.220
NanoGd2%	0.085
NanoGd10%	0.084

LCP: Luminescent-conjugated polythiophene.

were short, in the ranges 513 ± 8 and 479 ± 10 ps for the nanoGd10% and nanoGd2% variants, respectively, somewhat faster than recorded for pFTAA in phosphate-buffered saline (565 ± 8 ps), in agreement with the above observation. The study was complemented by measurements of the QE using the slope method [13], presented in Table 1. For the PEG-LCP, the QE was similar to the value reported for pFTAA (0.21). Despite a lower QE in the case of the surface-grafted probes compared with the free polymer, the results showed that no further quenching of the luminescence was observed when grafting density increased from 2 to 10%, confirming that the overall optical properties of the polythiophene units are not affected by the grafting. One should keep in mind that upon binding of LCP to Aβ aggregates, the excitation spectrum shifts to considerably longer wavelengths, making the apparent QE (overall apparent brightness) higher when examining LCP–amyloid aggregates by fluorescence microscopy [23]. Moreover, as previously demonstrated on our first generation of LCP-grafted nanoGd, TPA excitation using laser scanning fluorescence microscopy can dramatically reduce tissue autofluorescence [9]. This was also the case using the new nanoGd variants: in Supplementary Figure 6 are shown representative hyperspectral microscopy images and associated emission spectra, taken upon TPA excitation at 800 nm of *in vivo* stained sections. Taken together, the spectroscopic results and hyperspectral imaging allowed us to conclude that the grafted nanoparticles have very similar optical properties to the free LCP variants, specifically pFTAA [23].

The potential of NanoGd2% and NanoGd10% to be used as contrast media for MRI was further evaluated with the measurement of their relaxivities (Supplementary Table 1). Although the results obtained were in the same ranges of r_1 and r_2 values, slight variations were still observed, with higher relaxivities for NanoGd10% compared with NanoGd2%. In fact, due to the important length of the LCP polymer, the amount grafted on the particles might have an impact on the tumbling rate, which could explain the higher values observed for NanoGd10% compared with NanoGd2%. Importantly, despite these variations, the ratio r_2/r_1 of both NanoGds was similar (193–194) and, importantly, more than double that of commercially available iron oxide nanoparticles (83) which are known to be efficient T2/T2* contrast agents.

In summary, compared with our initial hybrid Nano GdF_3 contrast agent [9], the nanoparticles were successfully functionalized with a pentameric LCP (grafted at 2 and 10%) able to bind to a wider variety of Aβ plaque morphologies than the previously used q-FTAA (grafted at 5%). The resulting contrast agents were in the same size range (50–70 nm diameter) and retained both fluorescent properties and high relaxivity, making them suitable for *in vivo* evaluation.

Biodistribution in naive animals

Biodistribution of the nanoprobes was evaluated after injection of their suspension in physiological serum (150 µmol Gd/kg) in the tail vein of mice during dynamic 7T MRI of the abdomen (Figure 4). Results from NanoGd10% (n = 2) and NanoGd2% (n = 2) were pooled because both contrast agents displayed the same pharmacokinetics in these wild-type animals. We observed a moderate enhancement over time in the kidneys, which may indicate glomerular elimination (T1 effect). In parallel, the liver and spleen curves dropped and stabilized at around 40% and 20% below their initial level, respectively, which might reflect the uptake of the nanoparticles by the reticuloendothelial system (T2* effects). In contrast, MRI signals from a large vessel (abdominal aorta, Supplementary Figure 7) showed an initial signal drop and recovery (T2* effect due to susceptibility effects on this gradient echo sequence). Afterward, there was no major decay of the blood signal, which reflects the slow vascular clearance (and hence long vascular retention) of the nanoprobes.

Evaluation of targeting in AD models

The ability of NanoGd probes to bind Aβ aggregates *in vivo* was first evaluated in a rat model with stereotaxic injection of synthetic Aβ fibrils. Because the probe had to be delivered through a direct intracerebral injection, only the more stable (less susceptible to form aggregates) NanoGd10% was used for this proof-of-concept experiment. As previously described [14], animals were first injected with 5 µl of preformed $Aβ_{42}$ fibrils unilaterally in the right dentate gyrus. This was immediately followed by bilateral injections of NanoGd10% (2.5 µl at 140 µM, 55 ng of Gd) in right and left hippocampi. *In vivo* MRI was performed within 1 h after the injections and followed by intracardiac perfusion of the animal. Subsequently excised brain was conditioned for *ex vivo* phase-contrast tomography (XPCI). Figure 5 summarizes *in vivo* MRI and *ex vivo* PCT observations. Both MRI and PCT showed bilateral signals in cortex along the injection tracks (red arrows), revealing partial leakage of NanoGd10% on both sides. However, only the Aβ-injected right hippocampus displayed a negative MRI signal and positive PCT signal along the dentate gyrus (yellow arrows), suggesting that the contrast agent was bound to fibrils on this side while it quickly washed out on the contralateral left side. Hence this simplified animal model evidenced the possibility to image the probe targeting Aβ fibrils with two complementary modalities.

Additional MRI experiments were performed in two rats which received an intravenous injection of NanoGd10% (50 µmol Gd/kg) 2 and 7 days, respectively, after the intracerebral injection of Aβ fibrils. No signal was detected *in vivo* with MRI. Faint fluorescence was observed on postmortem examination (not shown). The inability to detect NanoGd10% after intravenous injection was interpreted as a limited BBB passage in rats which prevented sufficient binding and *in vivo* detection.

To evaluate this hypothesis, we administered NanoGd 3 h post-ictus in a mouse model of focal brain injury that induces opening of the BBB (Figure 6) [24]. After injection of 150 µmol Gd/kg (NanoGd10%, n = 3), MR images showed a moderate enhancement (up to 10%) in cortical areas submitted to BBB damage (T1 effects), while in the contralateral area the MR signal slightly and transiently dropped due to the presence of nanoprobes in the microcirculation (T2* effects). These results highlighted the ability of the nanoparticle to diffuse in areas where the BBB is disrupted and generate enough contrast to observe the cerebral lesion. Furthermore, after sacrifice of these animals, biphoton imaging was performed on excised organs (liver, brain), as shown in Supplementary Figure 8, and confirmed the presence of the LCP-grafted moiety onto the nanoparticles, suggesting the stability of the probes and a cellular uptake 1 h after injection.

The next evaluation step was thus performed in transgenic mice, which represent a more physiological animal model of AD pathology. The ability of the probes to specifically target the aggregates was evaluated through TPM imaging *in vivo*. The binding of NanoGd2% and NanoGd10% to Aβ plaques was monitored on two APPPS1 mice (11 months of age) equipped with a cranial window. Imaging was carried out with a two-photon microscope after injection of the probes (200 µmol Gd/kg) in the tail vein. Dynamic imaging was performed before injection and up to 11 h after injection (Figure 7). Before injection of the particle suspension, baseline images only showed background tissue fluorescence of the cortical area of study (Figure 7A & C). The presence

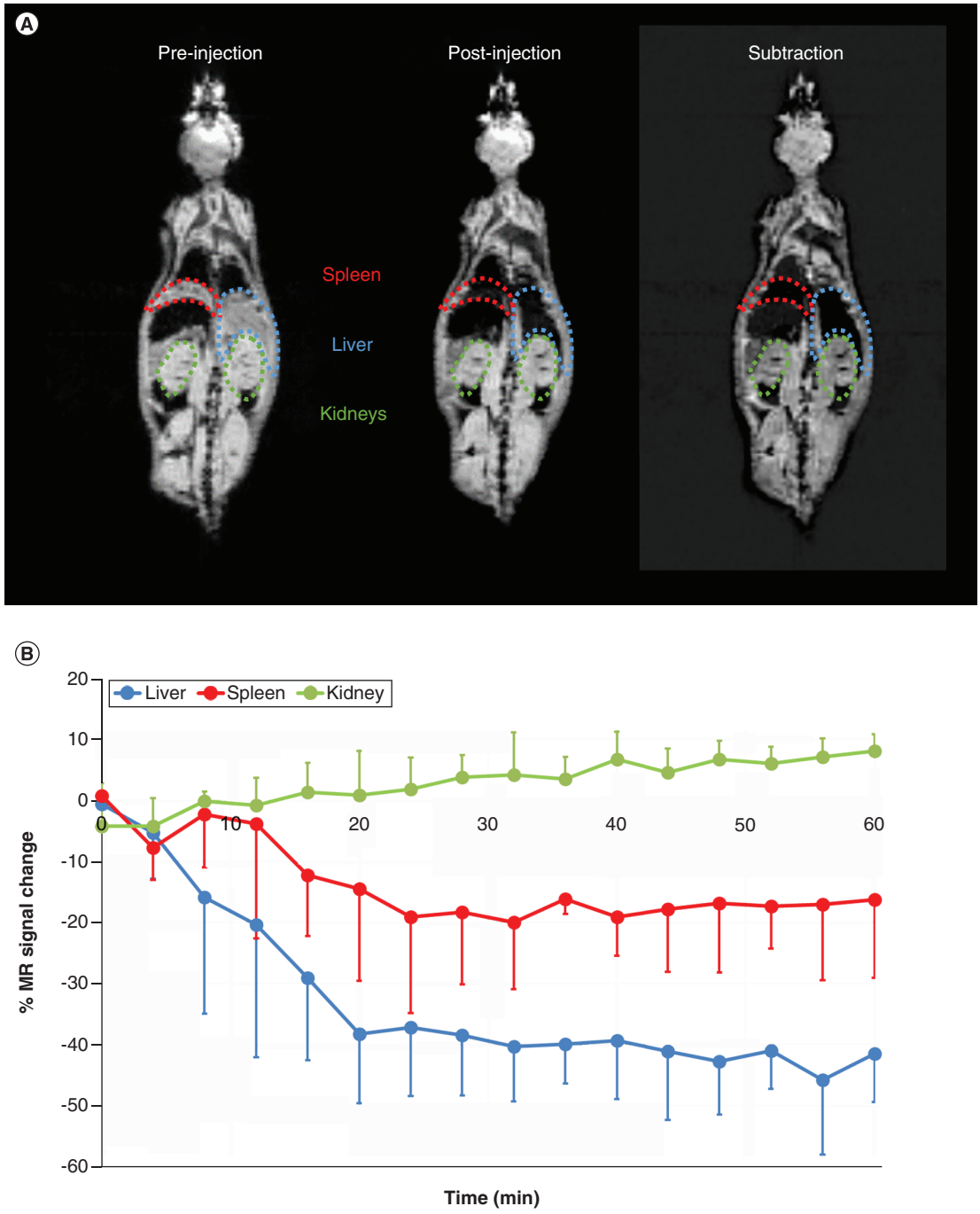

Figure 4. **(A)** Representative images of mouse abdomen before and after nanoGd injection and resulting subtraction (pre minus post) image. **(B)** Quantification of MRI signals measured in liver, spleen and kidney, averaged (mean ± standard deviation) from four animals (n = 2, NanoGd10% and n = 2, NanoGd2%).

of NanoGd2% and NanoGd10% was observed in the blood vessels immediately after injection (red arrows) and the brain vascularization was clearly identified. After 5 h, staining of the Aβ plaque fibrillar material was observed, with a contrast enhancement localized outside of the blood vessels (yellow arrows). The vascular lumen was still visible, confirming the long retention of the probes in the blood pool. After 11 h, NanoGd10% displayed higher Aβ plaque-related fluorescence than NanoGd2%. Measurements of the fluorescence intensity were in agreement with these visual observations. A strong enhancement was observed with both nanoprobes within the first hour after the injection (Figure 7B & D, green line). Slow fading of the fluorescence occurred in the blood, while the

10.2217/nnm-2022-0252

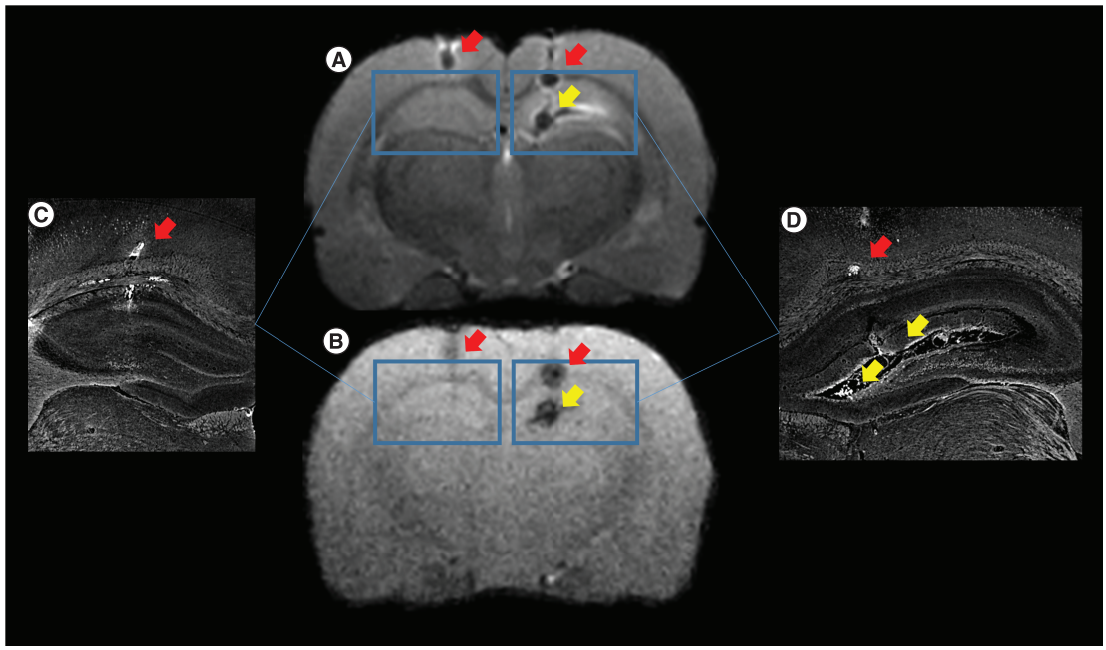

Figure 5. *In vivo* **(A)** T2-weighted and **(B)** T1-weighted MRI after intracerebral injection of NanoGd10%. **(C & D)** *Ex vivo* phase-contrast tomography images (maximum intensity projections over three slices at the level of dentate gyrus) are shown as corresponding inserts: **(C)** with NanoGd10% alone) and **(D)** with Aβ fibrils and NanoGd10%. Red arrows indicate nanoparticles detected along the injection tracks on both sides; yellow arrows indicate nanoparticles detected at amyloid-β fibril injection site.

intensity increased in the Aβ plaques. For both nanoprobes, the Aβ plaques were unambiguously detected after 3 h, when fluorescence intensity reached higher levels than in the vessels. Interestingly, after 3 h, the Aβ signal stabilized in the case of NanoGd2% while increasing continuously with NanoGd10%, up to 11 h. This difference suggests a more efficient targeting of the probe, probably due to the higher amount of LCP polymer. Finally, the fluorescence intensity measured in the brain parenchyma remained low and constant over the whole experiment, showing low nonspecific retention in cerebral tissue. These results proved the efficiency of NanoGd to target Aβ plaques after systemic injection. The clear Aβ plaque enhancement in the brain parenchyma evidenced the ability of the nanoprobes to cross the BBB. However, the BBB is likely to be dysfunctional in these aged transgenic animals, which might allow passive extravasation of the particles [25].

Finally, specific location of the probe within the brain parenchyma after Aβ plaque targeting was confirmed with high-resolution TPA spectral imaging, performed *ex vivo* on brain sections (Supplementary Figure 8). Specific spectra of the probes were obtained from ROIs corresponding to the Aβ plaques, and the results confirmed the dynamic observation that the probes are able to transfer from the bloodstream to the brain tissue, allowing specific imaging of the Aβ plaques. Spectra of various ROIs showed the same profile whatever the probes injected – NanoGd2% (Supplementary Figure 9E) or NanoGd10% (Supplementary Figure 9C) – with a maximum of emission centered at 540 nm. The loading of LCP moieties (NanoGd2% or NanoGd10%), however, had an impact on the emission intensity: NanoGd2% exhibited lower intensity than NanoGd10% while no differences in terms of targeting efficiency were observed.

Discussion

After our initial description of a new multimodal fluorescent magnetic hybrid nanoprobe [9], we here introduced an optimized, second-generation system with LCP under its pentameric form. In contrast to most recent studies [6,26–28], including ours [9], which reported only *ex vivo* imaging, this work focuses on multimodal *in vivo* evaluation in various animal models to better catch the translational potential of this probe. Indeed, we combined MRI and TPM, as well as *ex vivo* 3D detection with synchrotron XPCI.

A key challenge for nanoparticle-based agents targeting the brain is the brain uptake and crossing of the BBB. A recent review estimated that no more than 4% of metallic-based nanoparticles administered (per gram of tissue)

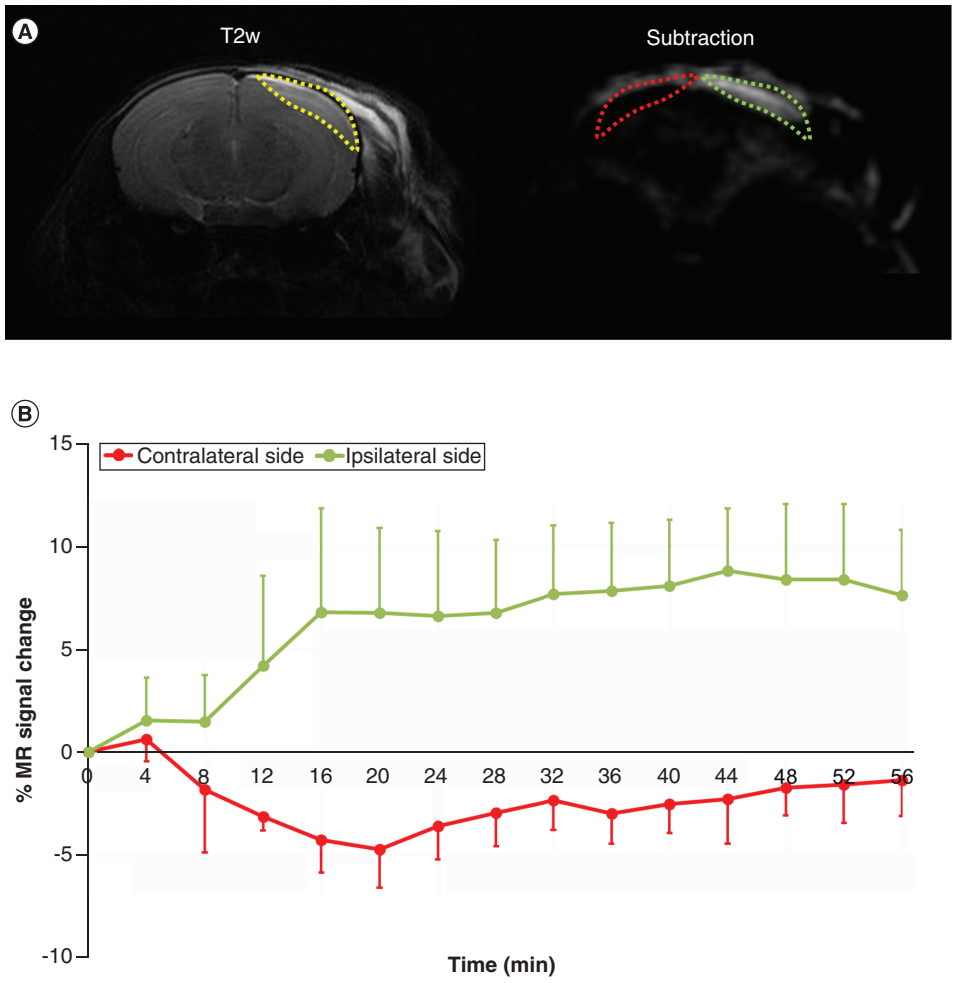

Figure 6. **(A)** Representative images of mouse brain highlighting the hyperintense cortical lesion (right panel, yellow outline), and subtraction image (post minus pre) obtained after intravenous injection of NanoGd10% (left panel). **(B)** MRI signal changes measured (mean ± standard deviation; n = 3) in the lesion (ipsilateral side, green outline and curve) and in the symmetrical region (contralateral, red outline and curve).

usually cross the BBB [29]. In recent systematic reviews focusing on AD, crossing the BBB without disrupting its integrity was also identified as the main challenge for magnetic nanoparticles [30], as well as for other nanostructures such as quantum dots [31] or fluorescent nanoprobes [32]. From our combination of animal models and imaging modalities, it appears that cerebral uptake and subsequent *in vivo* detection are dependent on the BBB status: detection can be achieved locally with highly sensitive two-photon fluorescence microscopy in APPPS1 mice with dysfunctional BBB, while less sensitive MRI detection requires extended BBB rupture or direct intracerebral injection. This gap in sensitivity requirement was also noted for other Aβ agents, like nanobodies linked to gadolinium chelates [33,34], or PBCA nanoparticles [35]. While there is no efficient strategy described to massively increase the cerebral uptake of nanoparticles [29], a compromise has to be found between increasing the sensitivity through a higher gadolinium load and designing small and furtive agents that are able to circulate long enough to reach the brain compartment. Alternatively, intranasal delivery could prove more efficient than intravenous injections, having been successfully tested with magnetite [36] and chitosan [37] nanoparticles.

The use of gadolinium-based nanoparticles is less widespread than that of iron oxide nanoparticles. However, gadolinium is the only heavy metal suitable both for MRI enhancement and k-edge imaging, which uses an element-specific increase in x-ray absorption for an energy (K-band). This means that such gadolinium-based nanoparticles can be used with emerging spectral computed tomography technologies [38]. We already demonstrated the adaptation of this type of gadolinium-based contrast agent for spectral photon counting computed tomography imaging [39]. Moreover, the same nanoparticle, when devoid of LCP (without amyloid targeting), proved useful for the imaging

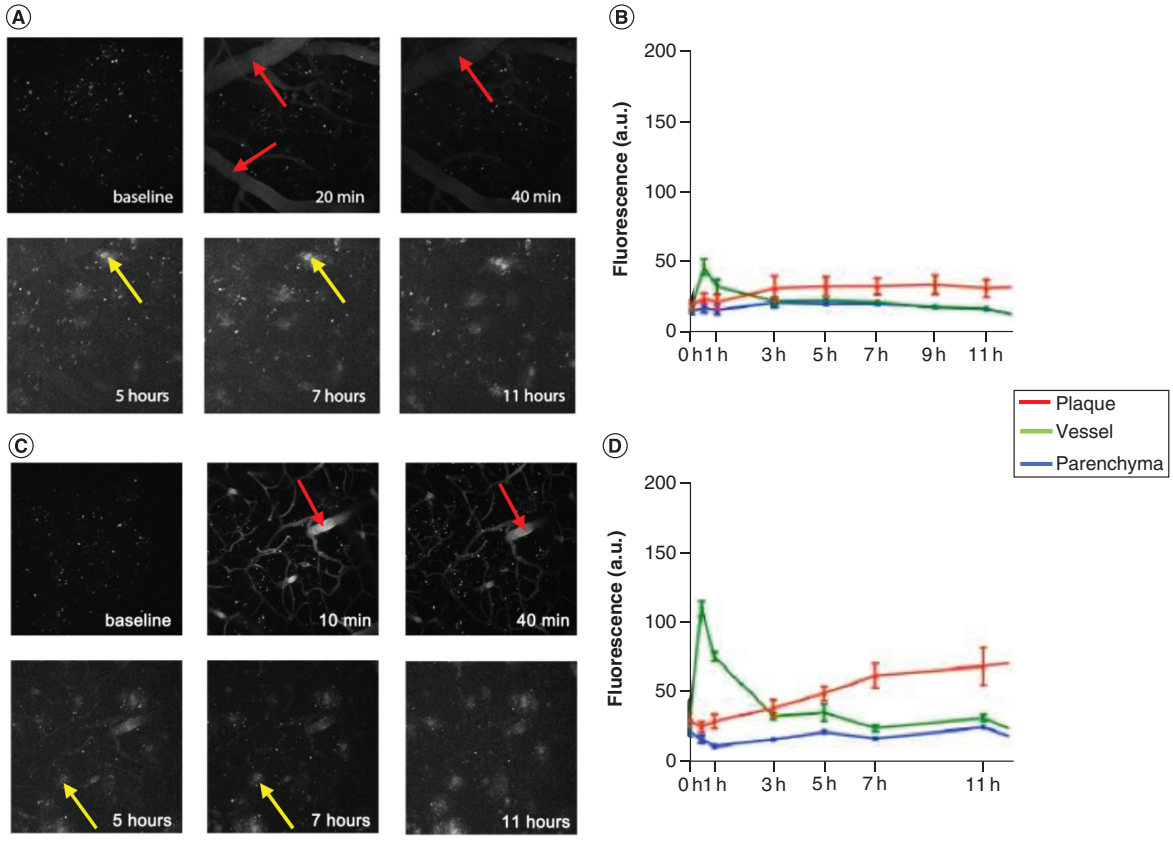

Figure 7. **(A)** Two-photon brain imaging after injection of NanoGd2%. **(B)** Monitoring of fluorescence intensity in various tissues with NanoGd2%. **(C & D)** The same results obtained with NanoGd10%. Red arrows show blood vessels, yellow arrows show amyloid-β plaques.

of neuroinflammation [40]. That study and the present one thus illustrate the translational potential of these versatile GdF_3 nanoparticles for multimodal imaging in animal models and possibly in a clinical setting.

Among Aβ-targeting ligands commonly used to functionalize nanoparticles, like Congo red [5] or curcumin [6], LCPs hold great potential for their ability to provide a spectral signature of different Aβ conformational variants [8], which might be considered as the molecular basis for different disease subtypes. Hence a collection of NanoGd nanoparticles functionalized with a series of LCPs would allow us to dissect *in vivo* the mechanisms of seeding and spreading of the prion-like Aβ pathology.

Conclusion

We provided the first example of successful targeting using a new class of GdF_3 nanoparticles. We performed proof-of-concept *in vivo* imaging experiments with TPM and MRI, which highlighted Aβ targeting in both transgenic mice and fibril-injected rats. Higher grafting (10 vs 2%) seemed to provide better stability and more sensitive detection without changing the overall biodistribution. In addition, we showed that NanoGd nanoparticles are suitable for postmortem virtual histology using high-resolution phase-contrast tomography, hence paving the road to an additional use for (spectral) computed tomography.

Supplementary data

To view the supplementary data that accompany this paper please visit the journal website at: www.futuremedicine.com/doi/suppl/10.2217/nnm-2022-0252

Author contributions

Frédéric Lerouge: conceptualization; methodology; validation; writing – original draft; investigation; supervision. E Ong: methodology; formal analysis; investigation. H Rositi: formal analysis; investigation. F Pambani: formal analysis; investigation. L-P Berner:

Summary points

- Successful targeting of amyloid-β is achieved using a new class of GdF_3 nanoparticles.
- Gadolinium core allows both MRI and x-ray detection.
- Pentameric luminescent-conjugated polythiophene ensures amyloid-β targeting and fluorescent detection.
- Proof of concept is provided using *in vivo* imaging in two animal models of Alzheimer's disease (transgenic mice and fibril-injected rats).
- Brain entry depends on blood–brain barrier status.

formal analysis; investigation. R Bolbos: investigation; writing – review and editing. C Olivier: investigation. F Peyrin: resources. V Apputukan: formal analysis; investigation. C Monnereau: conceptualization; investigation; methodology; writing – review and editing. C Andraud: validation. F Chaput: conceptualization; investigation; methodology. Y Berthezène: funding acquisition. B Braun: investigation; methodology. M Jucker: conceptualization; methodology. A Åslund: investigation. S Nyström: investigation. P Hammarström: project administration. P Nilsson: resources. M Lindgren: conceptualization; investigation; methodology; visualization; writing – review and editing. M Wiart: conceptualization; methodology; data curation; writing – review and editing; visualization; supervision; funding acquisition; project administration. F Chauveau: conceptualization; methodology; validation; writing – original draft; visualization; supervision. S Parola: conceptualization; methodology; validation; writing – review and editing; supervision; project administration; funding acquisition.

Acknowledgments

The authors would like to thank the following: J-B Langlois of the Animage platform (CERMEP, Lyon) for technical assistance during MRI experiments; M Wideroe (NTNU, Trondheim, Norway) for relaxivity measurements; A Durand (CREATIS, Lyon, France) for animal surgeries; B van der Sanden (Univ. Grenoble, France) for TPM on excised organs. They also thank ESRF for allocation of beamtime (LS2292) and E Boller from ID19 beamline for scientific and technical assistance. Biphosphonates were provided by Surfactis.

Financial & competing interests disclosure

The LUPAS project, FP7 Health (Call Reference no. FP7-HEALTH-2009-1.2-5, project no. 242098) is acknowledged for financial support. This research was also funded by the French national research agency (ANR) project NanoBrain (grant no. ANR-15-CE18-0026-01). The authors have no other relevant affiliations or financial involvement with any organization or entity with a financial interest in or financial conflict with the subject matter or materials discussed in the manuscript apart from those disclosed.

No writing assistance was utilized in the production of this manuscript.

Ethical conduct of research

The authors state that they have obtained appropriate institutional review board approval or have followed the principles outlined in the Declaration of Helsinki for all human or animal experimental investigations.

Government employee declaration

S Parola is an employee of the French research ministry.

References

Papers of special note have been highlighted as: • of interest; •• of considerable interest

1. Mathis CA, Mason NS, Lopresti BJ, Klunk WE. Development of positron emission tomography β-amyloid plaque imaging agents. *Semin. Nucl. Med.* 42(6), 423–432 (2012).
2. Azria D, Blanquer S, Verdier J-M, Belamie E. Nanoparticles as contrast agents for brain nuclear magnetic resonance imaging in Alzheimer's disease diagnosis. *J. Mater. Chem. B* 5(35), 7216–7237 (2017).
3. Pansieri J, Gerstenmayer M, Lux F *et al.* Magnetic nanoparticles applications for amyloidosis study and detection: a review. *Nanomaterials* 8(9), 740 (2018).
4. Wadghiri YZ, Li J, Wang J *et al.* Detection of amyloid plaques targeted by bifunctional USPIO in Alzheimer's disease transgenic mice using magnetic resonance microimaging. *PLoS ONE* 8(2), e57097 (2013).
5. Hu B, Dai F, Fan Z, Ma G, Tang Q, Zhang X. Nanotheranostics: Congo red/rutin-MNPs with enhanced magnetic resonance imaging and H_2O_2-responsive therapy of Alzheimer's disease in APPswe/PS1dE9 transgenic mice. *Adv. Mater.* 27(37), 5499–5505 (2015).
6. Cheng KK, Chan PS, Fan S *et al.* Curcumin-conjugated magnetic nanoparticles for detecting amyloid plaques in Alzheimer's disease mice using magnetic resonance imaging (MRI). *Biomaterials* 44, 155–172 (2015).

7. André S, Ansciaux E, Saidi E *et al.* Validation by magnetic resonance imaging of the diagnostic potential of a heptapeptide-functionalized imaging probe targeted to amyloid-β and able to cross the blood–brain barrier. *J. Alzheimers Dis.* 60(4), 1547–1565 (2017).
8. Rasmussen J, Mahler J, Beschorner N *et al.* Amyloid polymorphisms constitute distinct clouds of conformational variants in different etiological subtypes of Alzheimer's disease. *Proc. Natl Acad. Sci. USA* 114(49), 13018–13023 (2017).
9. Mpambani F, Åslund AKO, Lerouge F *et al.* Two-photon fluorescence and magnetic resonance specific imaging of Aβ amyloid using hybrid nano-GdF_3 contrast media. *ACS Appl. Biol. Mater.* 1(2), 462–472 (2018).

• **Seminal study describing the GdF_3 nanoprobe.**

10. Klingstedt T, Blechschmidt C, Nogalska A *et al.* Luminescent conjugated oligothiophenes for sensitive fluorescent assignment of protein inclusion bodies. *Chembiochem* 14(5), 607–616 (2013).

• **Comparison of luminescent-conjugated polythiophenes for targeting of brain amyloids.**

11. Chaput F, Lerouge F, Tusseau-Nenez S *et al.* Rare earth fluoride nanoparticles obtained using charge transfer complexes: a versatile and efficient route toward colloidal suspensions and monolithic transparent xerogels. *Langmuir* 27(9), 5555–5561 (2011).
12. Srour H, Ratel O, Leocmach M *et al.* Mediating gel formation from structurally controlled poly(electrolytes) through multiple 'head-to-body' electrostatic interactions. *Macromol. Rapid Commun.* 36(1), 55–59 (2015).
13. Crosby GA, Demas JN. Measurement of photoluminescence quantum yields. *Rev. J. Phys. Chem.* 75(8), 991–1024 (1971).
14. Verdurand M, Chauveau F, Daoust A *et al.* Differential effects of amyloid-β 1-40 and 1-42 fibrils on 5-HT1A serotonin receptors in rat brain. *Neurobiol. Aging* 40, 11–21 (2016).
15. Radde R, Bolmont T, Kaeser SA *et al.* $Aβ_{42}$-driven cerebral amyloidosis in transgenic mice reveals early and robust pathology. *EMBO Rep.* 7(9), 940–946 (2006).
16. Marinescu M, Langer M, Durand A *et al.* Synchrotron radiation x-ray phase micro-computed tomography as a new method to detect iron oxide nanoparticles in the brain. *Mol. Imaging Biol.* 15(5), 552–559 (2013).
17. Karpati S, Hubert V, Hristovska I *et al.* Hybrid multimodal contrast agent for multiscale *in vivo* investigation of neuroinflammation. *Nanoscale* 13(6), 3767–3781 (2021).
18. Paganin D, Mayo SC, Gureyev TE, Miller PR, Wilkins SW. Simultaneous phase and amplitude extraction from a single defocused image of a homogeneous object. *J. Microsc.* 206(1), 33–40 (2002).
19. Mirone A, Brun E, Gouillart E, Tafforeau P, Kieffer J. The PyHST2 hybrid distributed code for high speed tomographic reconstruction with iterative reconstruction and a priori knowledge capabilities. *Nucl. Instrum. Methods Phys. Res. Sect. B* 324, 41–48 (2014).
20. Rositi H, Frindel C, Wiart M *et al.* Computer vision tools to optimize reconstruction parameters in x-ray in-line phase tomography. *Phys. Med. Biol.* 59(24), 7767–7775 (2014).
21. Hefendehl JK, Wegenast-Braun BM, Liebig C *et al.* Long-term *in vivo* imaging of β-amyloid plaque appearance and growth in a mouse model of cerebral β-amyloidosis. *J. Neurosci.* 31(2), 624–629 (2011).
22. Hefendehl JK, Milford D, Eicke D *et al.* Repeatable target localization for long-term *in vivo* imaging of mice with 2-photon microscopy. *J. Neurosci. Methods* 205(2), 357–363 (2012).
23. Aslund A, Sigurdson CJ, Klingstedt T *et al.* Novel pentameric thiophene derivatives for *in vitro* and *in vivo* optical imaging of a plethora of protein aggregates in cerebral amyloidoses. *ACS Chem. Biol.* 4(8), 673–684 (2009).
24. Chauveau F, Moucharrafie S, Wiart M *et al. In vivo* MRI assessment of permanent middle cerebral artery occlusion by electrocoagulation: pitfalls of procedure. *Exp. Transl. Stroke Med.* 2(1), 4 (2010).
25. Ahn K-C, Learman CR, Dunbar GL *et al.* Characterization of impaired cerebrovascular structure in APP/PS1 mouse brains. *Neuroscience* 385, 246–254 (2018).
26. Plissonneau M, Pansieri J, Heinrich-Balard L *et al.* Gd-nanoparticles functionalization with specific peptides for ß-amyloid plaques targeting. *J. Nanobiotechnology* 14(1), 60 (2016).
27. Pansieri J, Plissonneau M, Stransky-Heilkron N *et al.* Multimodal imaging Gd-nanoparticles functionalized with Pittsburgh compound B or a nanobody for amyloid plaques targeting. *Nanomedicine* 12(14), 1675–1687 (2017).
28. Skaat H, Corem-Salkmon E, Grinberg I *et al.* Antibody-conjugated, dual-modal, near-infrared fluorescent iron oxide nanoparticles for antiamyloidgenic activity and specific detection of amyloid-β fibrils. *Int. J. Nanomedicine* 8(1), 4063–4076 (2013).
29. Ross AM, McNulty D, O'Dwyer C, Grabrucker AM, Cronin P, Mulvihill JJE. Standardization of research methods employed in assessing the interaction between metallic-based nanoparticles and the blood–brain barrier: present and future perspectives. *J. Control. Release* 296, 202–224 (2019).

•• **A systematic review of the methods by which metallic-based nanoparticles are characterized and assessed *in vivo*.**

30. Ulanova M, Poljak A, Wen W *et al.* Nanoparticles as contrast agents for the diagnosis of Alzheimer's disease: a systematic review. *Nanomedicine* 15(7), 725–743 (2020).

•• **Includes 33 studies of various nanoparticles for Alzheimer's disease imaging, with comparison of coating, functionalization, MRI relaxivity, toxicity and bioavailability.**

31. Villalva MD, Agarwal V, Ulanova M, Sachdev PS, Braidy N. Quantum dots as a theranostic approach in Alzheimer's disease: a systematic review. *Nanomedicine* 16(18), 1595–1611 (2021).
32. Lin J, Li H, Guo J *et al.* Potential of fluorescent nanoprobe in diagnosis and treatment of Alzheimer's disease. *Nanomedicine* 17(17), 1191–1211 (2022).
33. Li T, Vandesquille M, Koukouli F *et al.* Camelid single-domain antibodies: a versatile tool for *in vivo* imaging of extracellular and intracellular brain targets. *J. Control. Release* 243, 1–10 (2016).
34. Vandesquille M, Li T, Po C *et al.* Chemically-defined camelid antibody bioconjugate for the magnetic resonance imaging of Alzheimer's disease. *mAbs* 9(6), 1016–1027 (2017).
35. Koffie RM, Farrar CT, Saidi L-J, William CM, Hyman BT, Spires-Jones TL. Nanoparticles enhance brain delivery of blood–brain barrier-impermeable probes for *in vivo* optical and magnetic resonance imaging. *Proc. Natl Acad. Sci. USA* 108(46), 18837–18842 (2011).
36. Viola KL, Sbarboro J, Sureka R *et al.* Towards non-invasive diagnostic imaging of early-stage Alzheimer's disease. *Nat. Nanotechnol.* 10(1), 91–98 (2015).
37. El-Ganainy SO, Gowayed MA, Agami M *et al.* Galantamine nanoparticles outperform oral galantamine in an Alzheimer's rat model: pharmacokinetics and pharmacodynamics. *Nanomedicine* 16(15), 1281–1296 (2021).
38. Getzin M, Garfield JJ, Rundle DS *et al.* Increased separability of K-edge nanoparticles by photon-counting detectors for spectral micro-CT. *J. X-ray Sci. Technol.* 26(5), 707–726 (2018).
39. Halttunen N, Lerouge F, Chaput F *et al.* Hybrid nano-GdF_3 contrast media allows pre-clinical *in vivo* element-specific K-edge imaging and quantification. *Sci. Rep.* 9(1), 12090 (2019).
40. Hubert V, Hristovska I, Karpati S *et al.* Multimodal imaging with nanoGd reveals spatiotemporal features of neuroinflammation after experimental stroke. *Adv. Sci. (Weinh.)* 8(17), e2101433 (2021).

•• **First report to decipher the working mechanism of magnetic resonance signals induced by a nanoparticle passively targeted at phagocytic cells by performing intravital microscopy back-to-back with MRI.**